https://doi.org/10.5194/amt-2020-51
Preprint. Discussion started: 12 May 2020

Atmospheric Measurement Techniques Discussions

Quantifying the impact of aerosol scattering on the retrieval of methane from airborne remote sensing measurements

Yunxia Huang[1,2], Vijay Natraj[3], Zhaocheng Zeng[2,4], and Yuk L. Yung[2,3]

[1]School of Science, Nantong University, Nantong, 226007, China
[2]Division of Geological and Planetary Sciences, California Institute of Technology, Pasadena, CA 91125, USA
[3]Jet Propulsion Laboratory, California Institute of Technology, Pasadena, CA 91109, USA
[4]Joint Institute for Regional Earth System Science and Engineering, University of California, Los Angeles, CA 90095, USA

Correspondence to: Vijay Natraj (vijay.natraj@jpl.nasa.gov)

Abstract. As a greenhouse gas with strong global warming potential, atmospheric methane (CH_4) emissions have attracted a great deal of attention. Remote sensing measurements can provide information about CH_4 sources and emissions. However, accurate assessment of CH_4 emissions is challenging due to the influence of aerosol scattering in the atmosphere. In this study, imaging spectroscopic measurements from the Airborne Visible/Infrared Imaging Spectrometer–Next Generation (AVIRIS-NG) in the short-wave infrared are used to analyze the impact of aerosol scattering on CH_4 retrievals. Using a numerically efficient two-stream-exact-single-scattering radiative transfer model, we also simulate AVIRIS-NG measurements for different scenarios and quantify the impact of aerosol scattering using two retrieval techniques — the traditional Matched Filter (MF) method and the Optimal Estimation (OE) method, which is a popular approach for trace gas retrievals. The results show that the MF method exhibits up to 50% lower fractional retrieval bias compared to the OE method at high CH_4 concentrations (>100% enhancement over typical background values) and is suitable for detecting strong CH_4 emissions, while the OE method is an optimal technique for diffuse sources (<50% enhancement), showing up to five times smaller fractional retrieval bias than the MF method. In addition, the impacts of aerosol scattering as a function of different parameters, such as surface albedo, CH_4 concentration, aerosol optical depth, single scattering albedo and asymmetry parameter, are also discussed.

https://doi.org/10.5194/amt-2020-51
Preprint. Discussion started: 12 May 2020

Atmospheric Measurement Techniques Discussions

1 Introduction

Atmospheric methane (CH_4) is about 85 times more potent per unit mass at warming the Earth than carbon dioxide (CO_2) on a 20-year timescale (IPCC, 2013), implying that reduction in CH_4 emissions could be very efficient to slow down global warming in the near term. Global mean CH_4 concentrations have increased from ~700 ppb in the preindustrial era to more than 1860 ppb as of 2019 (NOAA, 2019). The most effective sink of atmospheric CH_4 is the hydroxyl radical (OH) in the troposphere. CH_4 reacts with OH to reduce the oxidizing capacity of the atmosphere and generate tropospheric ozone. Increasing emissions of CH_4 reduce the concentration of OH in the atmosphere. With less OH to react with, the lifespan of CH_4 could also increase, resulting in greater CH_4 concentrations (Holmes et al., 2013). Soils also act as a major sink for atmospheric methane through the methanotrophic bacteria that reside within them.

Significant natural CH_4 sources include wetlands (Bubier et al., 1994, Macdonald et al., 1998; Gedney et al., 2004), geological seeps (Kvenvolden and Rogers, 2005; Etiope et al., 2009), ruminant animals, and termites. In addition, increased surface and ocean temperatures associated with global warming may increase CH_4 emissions from melting permafrost (Woodwell et al., 1998; Walter et al., 2006; Schaefer et al., 2014, Schuur et al., 2015) and methane hydrate destabilization (Kvenvolden, 1988; Archer, 2007). Human activity also contributes significantly to the total CH_4 emissions. Rice agriculture is one of the most important anthropogenic sources of CH_4 (Herrero et al., 2016; Schaefer et al., 2016). Other sources include landfills (Themelis and Ulloa, 2007), wastewater treatment, biomass burning, and methane slip from gas engines. Global fugitive CH_4 emissions from coal mining (Kort et al., 2014), natural gas and oil systems (Alvarez et al., 2018), hydraulic fracturing ("fracking") of shale gas wells (Howarth et al., 2011; Howarth, 2015, 2019), and residential and commercial natural gas distribution sectors (He et al., 2019) are also of increasing concern. Although the sources and sinks of methane are reasonably well known, there are large uncertainties in their relative amounts and in the partitioning between natural and anthropogenic contributions (Nisbet et al., 2014, 2016). This uncertainty is exemplified by the CH_4 "hiatus", which refers to the observed stabilization of atmospheric CH_4 concentrations from 1999–2006, and the renewed rise thereafter (Kirschke et al., 2013).

Visible/ShortWave InfraRed (VSWIR) imaging spectroscopy, also known as hyperspectral imaging, has been used for nearly four decades to remotely sense the Earth's surface and atmosphere. The 380–2500 nm spectral interval captures most of the solar energy, which is subject to absorption and scattering by the atmosphere and surface, thereby revealing diverse atmospheric and surface properties (Schaepman et al., 2009). Hyperspectral remote sensing has been utilized for research and applications in a variety of fields, including geology, agriculture, forestry, coastal and inland water studies, environment hazards

https://doi.org/10.5194/amt-2020-51
Preprint. Discussion started: 12 May 2020

Atmospheric Measurement Techniques Discussions

assessment, and urban studies. In order to study surface properties using imaging spectrometric data, atmospheric absorption and scattering effects need to be accounted for. The traditional method to do this is called atmospheric correction, which "removes" atmospheric effects and then converts radiances measured by the sensors to reflectances of surface materials. Operational atmospheric correction models include ATREM (Gao et al., 1993), ATCOR (Richter, 1996; Richter, 1998; Richter and Schläpfer, 2002), ISDAS (Staenz et al., 1998), HATCH (Qu et al., 2003), ACORN (Kruse, 2004) and FLAASH (Perkins et al., 2012). However, the process of atmospheric correction — where the atmosphere is retrieved first, followed by the surface — loses information about the atmosphere. Conversely, VSWIR spectral measurements contain information about atmospheric trace gases, aerosols, and thin cirrus clouds.

By combining large image footprints and fine spatial resolution, airborne imaging spectrometers are well suited for mapping local CH_4 plumes. The Airborne Visible/Infrared Imaging Spectrometer–Next Generation (AVIRIS-NG) measures reflected solar radiance across more than 400 channels between 380 and 2500 nm (Green et al., 1998; Thompson et al., 2015). Strong CH_4 absorption features present between 2100 and 2500 nm can be observed at a 5 nm spectral resolution and full width at half maximum (FWHM).

A number of approaches have been developed to retrieve CH_4 from hyperspectral data. Roberts et al. (2010) used a spectral residual approach between 2000 and 2500 nm and Bradley et al. (2011) employed a band ratio technique using the 2298 nm CH_4 absorption band and 2058 nm CO_2 absorption band. However, these techniques are not suited for terrestrial locations that have lower albedos and have spectral structure in the SWIR. A cluster-tuned matched filter technique was demonstrated to be capable of mapping CH_4 plumes from marine and terrestrial sources (Thorpe et al., 2013) as well as CO_2 from power plants (Dennison et al., 2013); however, this method does not directly quantify gas concentrations. Frankenberg et al. (2005) developed an iterative maximum *a posteriori* differential optical absorption spectroscopy (IMAP-DOAS) algorithm that allows for uncertainty estimation. Thorpe et al. (2014) adapted the IMAP-DOAS algorithm for gas detection in AVIRIS imagery. In addition, they developed a hybrid approach using singular value decomposition and IMAP-DOAS as a complementary method of quantifying gas concentrations within complex AVIRIS scenes.

Accurate assessment of CH_4 emissions is particularly challenging in the presence of aerosols because the latter introduce uncertainties in the light path if not accounted for. In fact, CH_4 emissions are frequently correlated with pollution due to concurrent aerosol emissions. For large aerosols (such as dust), the low Ångström exponent values result in high aerosol optical depth (AOD) values even in the wavelength range from 2000 nm to 2500 nm (Seinfeld and Pandis, 2006; Zhang et al., 2015). Therefore, it is important to obtain a clear understanding of aerosol impacts on CH_4 retrievals. In this study, SWIR AVIRIS-NG measurements are used to analyze the impact of aerosol scattering on CH_4 retrievals. Further,

https://doi.org/10.5194/amt-2020-51
Preprint. Discussion started: 12 May 2020


Atmospheric Measurement Techniques Discussions

using an accurate but numerically efficient radiative transfer (RT) model (Spurr and Natraj, 2011), we simulate AVIRIS-NG measurements with varying aerosol amounts and quantify the impact of aerosol scattering using two retrieval techniques, the traditional matched filter method and the optimal estimation method that is widely used in trace gas remote sensing.

2 Methods

2.1 Matched Filter (MF) method

Real-time remote detection using AVIRIS-NG measurements are traditionally based on the MF method (Frankenberg et al., 2016). In this method, the background spectra are assumed to be distributed as a multivariate Gaussian $\mathcal{N}$ with covariance matrix $\boldsymbol{\Sigma}$ and background mean radiance $\boldsymbol{\mu}$. If H_0 is a scenario without CH_4 enhancement and H_1 is one with CH_4 enhancement, the MF approach is equivalent to a hypothesis test between the two scenarios:

$$H_0: L_m \sim \mathcal{N}(\boldsymbol{\mu}, \boldsymbol{\Sigma}) \quad (1)$$

$$H_1: L_m \sim \mathcal{N}(\boldsymbol{\mu} + \boldsymbol{t}\alpha, \boldsymbol{\Sigma}) \quad (2)$$

where L_m is the measurement radiance; $\boldsymbol{t}$ is the target signature, which is defined in Equation (4); α is the enhancement value, denoting a scaling factor for the target signature that perturbs the background $\boldsymbol{\mu}$. If $\boldsymbol{x}$ is a vector of measurement spectra with one element per wavelength, $\alpha(\boldsymbol{x})$ can be written, based on maximum likelihood estimates (Manolakis et al., 2014), as follows:

$$\alpha(\boldsymbol{x}) = \frac{(\boldsymbol{x} - \boldsymbol{\mu})^T \boldsymbol{\Sigma}^{-1} \boldsymbol{t}}{\boldsymbol{t}^T \boldsymbol{\Sigma}^{-1} \boldsymbol{t}} \quad (3)$$

We utilize the same definitions as in Frankenberg et al. (2016). Specifically, the enhancement value $\alpha(\boldsymbol{x})$ denotes the thickness and concentration within a volume of equivalent absorption, and has units of ppm × m. The target signature $\boldsymbol{t}$ refers to the derivative of the change in measured radiance with respect to a change in absorption path length due to an optically thin absorbing layer of CH_4. Note that this definition has the disadvantage that the accuracy of the result degrades when the absorption is strong and further attenuation becomes nonlinear. At a particular wavelength λ, $\boldsymbol{t}$ can be expressed as:

$$\boldsymbol{t}(\lambda) = -\boldsymbol{\kappa}(\lambda)\boldsymbol{\mu}(\lambda), \quad (4)$$

where $\boldsymbol{\kappa}$ is the absorption coefficient for a near-surface plume with units of $\mathrm{ppm}^{-1}\,\mathrm{m}^{-1}$. This is different from the units of $\mathrm{m}^2 \cdot \mathrm{mol}^{-1}$ traditionally used for the absorption coefficient in trace gas remote sensing. Using the ideal gas law to express the volume V (in liters) occupied by one mole of CH_4 at the temperature and pressure corresponding to the plume altitude (V = 22.4 at standard temperature and pressure), and the relations 1 liter = $10^{-3}\,\mathrm{m}^3$ and 1 ppm = 10^{-6}, we obtain the following expression for unit conversion:

https://doi.org/10.5194/amt-2020-51
Preprint. Discussion started: 12 May 2020

Atmospheric Measurement Techniques Discussions

$$1\ \mathrm{m}^2 \cdot \mathrm{mol}^{-1} = \frac{1}{V \times 10^3}\ \mathrm{ppm}^{-1}\ \mathrm{m}^{-1} \quad (5)$$

Figure 1 presents the target signature, which is calculated based on HITRAN absorption cross-sections (Rothman et al., 2009). The background mean radiance $\boldsymbol{\mu}$ used is based on an AVIRIS-NG measurement made on 4 September 2014 (ang20140904t204546) in Bakersfield, CA. As shown in Figure 2, the samples for the background covariance matrix $\boldsymbol{\Sigma}$ and mean radiance $\boldsymbol{\mu}$ are drawn from the dashed green box near the CH_4 emission source, which is located within the solid red box.

2.2 Optimal Estimation (OE) method

The OE method is widely used for the remote sensing retrieval of satellite measurements, such as from the Orbiting Carbon Observatory-2 (OCO-2; O'Dell et al., 2018), the Spinning Enhanced Visible and Infra-Red Imager (SEVIRI; Merchant et al., 2013), and the Greenhouse Gases Observing Satellite (GOSAT; Yoshida et al., 2013). It combines an explicit (typically nonlinear) forward model of the atmospheric state, a (typically Gaussian) prior probability distribution for the variabilities and a (typically Gaussian) distribution for the spectral measurement errors. In addition, the Bayesian framework used by the OE approach allows new information (from measurements) to be combined with existing information (e.g., from models). In many applications, the forward model is nonlinear, and obtaining the optimal solution requires iterative techniques such as the Levenberg–Marquardt method (Rodgers, 2000), which has been routinely applied to study the impacts of measurement parameters on the retrieval process (see, e.g., Zhang et al., 2015). The iteration in this algorithm follows the below procedure.

$$\mathbf{x_{i+1}} = \mathbf{x_i} + [(1+\gamma)\mathbf{S_a^{-1}} + \mathbf{K_i^T S_\epsilon^{-1} K_i}]^{-1}\{\mathbf{K_i^T S_\epsilon^{-1}}[\mathbf{y} - \mathbf{F}(\mathbf{x_i})] - \mathbf{S_a^{-1}}[\mathbf{x_i} - \mathbf{x_a}]\} \quad (6)$$

where $\mathbf{x}$ is a state vector of surface and atmospheric properties, $\mathbf{S_a}$ is the *a priori* covariance matrix, $\mathbf{S_\epsilon}$ is the spectral radiance noise covariance matrix, $\mathbf{K}$ is the Jacobian matrix, $\mathbf{x_a}$ is the *a priori* state vector and γ is a parameter determining the size of each iteration step. The measured spectral radiance is denoted as $\mathbf{y}$; $\mathbf{F}(\mathbf{x})$ is the simulated radiance obtained from the forward model. For the retrieval of CH_4 from AVIRIS-NG measurements, the state vector includes the total column amounts of CH_4 and H_2O, while for the retrievals from synthetic spectra, the H_2O concentration is fixed and the state vector only includes the CH_4 total column. The *a priori* errors are assumed to be 20% for all state vector elements and the retrieved results are shown as the column averaged mixing ratio (XCH_4, in ppm).

3 Detection and retrieval of CH_4 from AVIRIS-NG measurements

https://doi.org/10.5194/amt-2020-51
Preprint. Discussion started: 12 May 2020

Atmospheric Measurement Techniques Discussions

Figure 2 shows a sample of CH_4 plume detection on 4 September 2014 by AVIRIS-NG. The location is to the west of the Kern Front Oil field. This detection is a case study from the NASA/ESA CO_2 and MEthane eXperiment (COMEX) campaign in California during June and August/September 2014, which includes airborne *in situ*, airborne non-imaging remote sensing, and ground-based *in situ* instruments to provide a real-time remote detection and measurement for CH_4 plumes released from anthropogenic sources. An RGB image of flight data is displayed in Figure 2a; the emission source is a pump jack, as described in Thompson et al. (2015). Figure 2b presents results from the MF method, which shows that the CH_4 plume disperses downwind and has a maximum enhancement value of about 2800 ppm × m. Some artifacts also produce large α values in the MF method; these can be removed by an optimization method such as the column-wise MF method (Thompson et al., 2015).

AVIRIS-NG provides measurements of reflected sunlight in the 380–2500 nm range with 5 nm spectral resolution; the 2100–2500 nm range with obvious CH_4 absorption features are often used to retrieve CH_4 enhancement. Figure 3 displays the measured radiance (a) before normalization and (b) after normalization, corresponding to two detector elements (in plume and out of plume). Every element is a cross-track spatial location. The radiance has units of $\mu W\ cm^{-2}\ nm^{-1}\ sr^{-1}$ and the wavelength spans the spectral range from 380 to 2500 nm. Comparing the measured spectrum in plume to that out of plume, there is obvious enhancement of CH_4 that is particularly evident in the normalized radiance. CH_4 is the main absorber in the 2100–2500 nm wavelength range, and H_2O is the major interfering gas. Figure 3b indicates the absorption peaks due to H_2O and CH_4.

We choose the plume center with 500 elements to illustrate results obtained using the MF and OE methods. The former evaluates the CH_4 α value compared to the background CH_4 concentration, while the latter retrieves XCH_4. Results for the latter are shown as a multiplicative scaling factor compared to a typical XCH_4 background of 1.822 ppm. We use an accurate and numerically efficient two-stream-exact-single-scattering (2S-ESS) RT model (Spurr and Natraj, 2011). This forward model is different from a typical two-stream model in that the two-stream approximation is used only to calculate the contribution of multiple scattering to the radiation field. Single scattering is treated in a numerically exact manner using all moments of the phase function. This model has been used for remote sensing of greenhouse gases and aerosols (Xi et al., 2015; Zhang et al., 2015, 2016; Zeng et al., 2017, 2018).

Results from the two retrieval methods (Figure 4) reveal a similar CH_4 plume shape, especially for elements with high CH_4 enhancement. However, larger differences in CH_4 concentrations are evident in the OE retrievals (Figure 4b). One reason is that, in the OE method, H_2O and CH_4 are simultaneously retrieved; the CH_4 retrieval has added uncertainty due to overlapping absorption features between these two gases. The large maximum value of about 3000 in the MF method also contributes to a reduction in

https://doi.org/10.5194/amt-2020-51
Preprint. Discussion started: 12 May 2020

Atmospheric Measurement Techniques Discussions

relative contrast. It is difficult to compare the CH_4 enhancement directly between the two methods since the background CH_4 concentration used in the MF method cannot be quantified exactly. Therefore, we simulate synthetic spectra (see section 4) using the 2S-ESS RT model to study the impacts of aerosol scattering as a function of different geophysical parameters.

4 Aerosol impact analysis

4.1 Synthetic spectra

In a real AVIRIS-NG observation, the exact column concentration of CH_4 cannot be controlled. However, synthetic simulations allow us to manipulate parameters such as CH_4 concentration, surface albedo, AOD, asymmetry parameter (g), and single scattering albedo (SSA), and thereby test aerosol impacts on CH_4 retrievals. The 2S-ESS RT model is used to simulate AVIRIS-NG spectral radiance. In this model, a prior atmospheric profile with 70 layers from the surface up to 70 km is derived from National Center for Environmental Prediction reanalysis data (Kalnay et al., 1996); absorption coefficients for all relevant gases are obtained from the HITRAN database (Rothman et al., 2009). Monochromatic RT calculations are performed at a spectral resolution of 0.5 cm^{-1}; the radiance spectrum is then convolved using a Gaussian instrument line shape function with a wavelength-dependent full width at half maximum (FWHM) from a calibrated AVIRIS-NG data file. The signal to noise ratio (SNR) is set to be 300, with Gaussian white noise added. This procedure results in a wavelength grid with a resolution of about 5 nm. The spectral wavelength range used to retrieve CH_4 is from 2100 nm to 2500 nm.

The additional atmospheric and geometric variables included in the model are listed in Table 1, which are held constant unless otherwise mentioned. The observation geometry parameters are taken from a real AVIRIS-NG measurement. Recent AVIRIS-NG fight campaigns have sensor heights ranging from 0.43 to 3.8 km; we choose a value of 1 km, the same as the highest level where aerosol is present in our simulations. The influence of AOD on CH_4 retrieval as a function of SSA and g is analyzed in Section 4.3; in all other cases, SSA and g are held constant at 0.95 and 0.75, respectively.

4.2 Aerosol impact in the MF method

We simulate synthetic spectra at different AOD, surface albedo and CH_4 concentration values, use the MF method to obtain the CH_4 enhancement, and compare differences in α between scenarios with and without aerosol. The covariance and mean radiance are calculated from a simulated zero AOD background with albedos from 0.1 to 0.5, and XCH_4 set at a typical background value of 1.822 ppm. Figure 5a shows the enhancement value as a function of XCH_4. As the CH_4 concentration increases, the

https://doi.org/10.5194/amt-2020-51
Preprint. Discussion started: 12 May 2020

Atmospheric Measurement Techniques Discussions

enhancement value obtained by the MF method at first increases approximately linearly. However, since the absorption cross-section changes in a nonlinear fashion with concentration, the enhancement value also becomes nonlinear at larger XCH_4. Two aerosol scenarios (AOD = 0, AOD = 0.3) are compared in Figure 5a, which reveals that the effect of aerosol loading is similar to an underestimation of CH_4 in the retrieval. The underestimation is clearly shown in Figure 5b, where the enhancement value for fixed CH_4 concentration (same concentration as the background) decreases from 0 ppm × m to −1532 ppm × m with increasing AOD. To clarify the impact of AOD at different surface albedo values, zoomed in versions of α as a function of XCH_4 are presented in Figures 5c, 5d, 5e and 5f. For the AOD = 0 scenario, the results are independent of surface albedo. For the scenarios with aerosol loading, the dispersion between the results at different surface albedos and the changes in the zero-enhancement value (relative to the background concentration of CH_4 = 1.0 × 1.822 ppm) indicates that results from the MF method are biased more at large AOD and surface albedo values; the maximum bias value is close to 0.06 × 1.822 ppm for an AOD of 0.3 and albedo of 0.5, as shown by the dotted line in Figure 5f.

A quantitative analysis of underestimation of CH_4 concentration due to aerosol scattering is presented in Figure 6. The color bar shows the α bias, which is defined as the difference between the enhancements without and with aerosols, for different CH_4 concentrations, surface albedos and AODs. The α bias increases with increasing surface albedo and AOD, reaching a maximum value of about 700 ppm × m for the simulated cases. However, it is interesting that the bias decreases with increasing CH_4 concentration, which is different from the results obtained by the OE method (discussed in section 4.3). This difference arises due to the nonlinear deviation at higher CH_4 concentrations using the MF method, as discussed earlier.

4.3 Aerosol impact in the OE method

For the simulation of the synthetic spectra, we assume nonzero aerosol loading below 1 km elevation. The OE method is then used to perform retrievals using the same configuration except that AOD is set to zero. This approach is similar to neglecting aerosol scattering in the CH_4 retrieval; the retrieval bias is defined as the difference between the true XCH_4 in the simulation (nonzero AOD) and the retrieved value (zero AOD).

It is of interest to study the retrieval bias caused by different aerosol types. We employ the Henyey-Greenstein phase function (Henyer and Greenstein, 1941), where aerosol composition is determined by two parameters: SSA and g. Figure 7 shows CH_4 retrieval biases as a function of SSA and g; surface albedo and AOD are kept constant at 0.3 and the XCH_4 is assumed to be 1.0 × 1.822 ppm. The retrieval bias increases with SSA and decreases with g, with a maximum bias ratio (ratio of retrieval bias to the

https://doi.org/10.5194/amt-2020-51
Preprint. Discussion started: 12 May 2020

Atmospheric Measurement Techniques Discussions

true value) of about 20%. Synthetic spectra are simulated for different values of CH_4 concentration, surface albedo and AOD. The impacts of aerosol scattering on the retrievals for these scenarios are demonstrated in Figure 8. Figure 8a shows a 5 × 5 panel of boxes. Within each box, XCH_4 is constant, while surface albedo increases from top to bottom and AOD increases from left to right. It is evident that the retrieved CH_4 bias increases with increasing AOD. The CH_4 bias induced by differences in the surface albedo is not as large as that due to AOD variations, but albedo effects are noticeable at large AOD. In contrast with the MF method, OE retrievals produce larger CH_4 biases at higher XCH_4 values. The variation of XCH_4 across the boxes is shown in Figure 8b. We also show a zoomed in plot of the bottom right box (XCH_4 = 5.8 × 1.822 ppm) in Figure 8c, which illustrates the AOD and surface albedo changes within a box. These changes are identical for all boxes.

4.4 Comparison of the two retrieval techniques

Figure 9 presents the bias ratios for the two retrieval techniques at different AODs. In the MF method, we assume the truth to be the retrieved α for the case with zero AOD. The bias ratio is therefore defined as the ratio of the bias in retrieved α to the true value of α. On the other hand, in the OE method, the bias ratio is the ratio of the retrieved XCH_4 difference (between scenarios without and with aerosol) to the real XCH_4. In all cases the surface albedo is set to 0.3. From Figure 9 it is clear that the bias ratio decreases with increasing CH_4 concentration and has higher values at larger AODs. The bias ratio for the MF method is up to 50% less than that for the OE method when the CH_4 concentration is high (>~2 × 1.822 ppm). On the other hand, the OE method performs better when enhancements are small and XCH_4 is close to the background value. For example, the bias ratio for the MF method has a high value of about 0.43 at AOD = 0.3 for a 10% enhancement (XCH_4 = 1.1 × 1.822 ppm); the OE value for the same scenario is 0.086. The two retrieval techniques seem to be complementary, with differing utilities for different enhancements.

5 Discussion

Remote sensing measurements from airborne and satellite instruments are widely used to detect CH_4 emissions. In our study, the traditional MF and the OE methods are used to quantify the effects of aerosol scattering on CH_4 retrievals based on simulations of AVIRIS-NG measurements. The results show that the retrieval biases increase with increasing AOD and albedo for both techniques. In the OE method the biases increase with increasing CH_4 concentration and SSA, but decrease with increasing aerosol asymmetry parameter. The CH_4 retrieval bias increases with increasing XCH_4 in the OE method but decreases for the same scenario in the MF method. The contrasting trend is attributed to nonlinear effects

https://doi.org/10.5194/amt-2020-51
Preprint. Discussion started: 12 May 2020

Atmospheric Measurement Techniques Discussions

at higher XCH_4 values in the MF method. We also present bias ratios for the two techniques. The MF method shows smaller bias ratios at large CH_4 concentrations than the OE method; it is, therefore, an optimal method to detect strong CH_4 emission sources. On the other hand, the OE method seems to be more suitable for detecting diffuse sources. Further, the MF method relies on a comparison with the background CH_4 concentration. It is difficult to get an accurate estimate of the background XCH_4 value in polluted atmospheric environments. In contrast, the OE method provides retrievals based solely on the atmospheric scenario of interest.

This study focused on a comparison of retrieval techniques. It is also important to accurately represent the physics of atmospheric RT, especially for scenarios with significant aerosol scattering. RT models traditionally used in retrievals of imaging spectroscopic data use simplified radiation schemes and predefined aerosol models, which may introduce inaccurate in the representation of atmospheric physics. The 2S-ESS model provides the capability to quantify aerosol impacts on CH_4 retrieval for different aerosol types, optical depths and layer heights. In future work, we will compare retrievals using the 2S-ESS model against other commonly used models such as MODTRAN. We will also evaluate the impact of varying instrument spectral resolution and signal to noise ratio for simultaneous retrieval of CH_4 and AOD. This will be relevant for the design of imaging spectrometers for planned future missions such as the NASA designated Surface Biology and Geology (SBG) mission.

Acknowledgements

A portion of this research was carried out at the Jet Propulsion Laboratory, California Institute of Technology, under a contract with the National Aeronautics and Space Administration (80NM0018D0004). V.N. acknowledges support from the NASA "Utilization of Airborne Visible/Infrared Imaging Spectrometer Next Generation Data from an Airborne Campaign in India" program (solicitation NNH16ZDA001N-AVRSNG), and the Jet Propulsion Laboratory Research and Technology Development program.

https://doi.org/10.5194/amt-2020-51
Preprint. Discussion started: 12 May 2020

317 **References**

318

319 Alvarez, R. A., Zavala-Araiza, D., Lyon, D. R., Allen, D. T., Barkley, Z. R., Brandt, A. R., Davis, K. J.,
320 Herndon, S. C., Jacob, D. J., Karion, A., Kort, E. A., Lamb, B. K., Lauvaux, T., Maasakkers, J. D.,
321 Marchese, A. J., Omara, M., Pacala, S. W., Peischl, J., Robinson, A. L., Shepson, P. B., Sweeney, C.,
322 Townsend-Small, A., Wofsy, S. C., and Hamburg, S. P.: Assessment of methane emissions from the U.S.
323 oil and gas supply chain, Science, 361, 186–188, https://doi.org/10.1126/science.aar7204, 2018.

324

325 Archer, D.: Methane hydrate stability and anthropogenic climate change, Biogeosci., 4, 521–544,
326 https://doi.org/10.5194/bg-4-521-2007, 2007.

327

328 Bradley, E. S., Leifer, I., Roberts, D. A., Dennison, P. E., and Washburn, L.: Detection of marine methane
329 emissions with AVIRIS band ratios, Geophys. Res. Lett., 38, L10702,
330 https://doi.org/10.1029/2011GL046729, 2011.

331

332 Bubier, J. L., and Moore, T. R: An ecological perspective on methane emissions from northern wetlands,
333 Trends in Ecology and Evolution, 9, 460–464, https://doi.org/10.1016/0169-5347(94)90309-3, 1994.

334

335 Dennison, P. E., Thorpe, A. K., Pardyjak, E. R., Roberts, D. A., Qi, Y., Green, R. O., Bradley, E. S., and
336 Funk, C. C.: High spatial resolution mapping of elevated atmospheric carbon dioxide using airborne
337 imaging spectroscopy: Radiative transfer modeling and power plant plume detection, Remote Sens.
338 Environ., 139, 116-129, https://doi.org/10.1016/j.rse.2013.08.001, 2013.

339

340 Earth System Research Laboratory Global Monitoring Division,
341 https://esrl.noaa.gov/gmd/ccgg/trends_ch4/, NOAA, 2019.

342

343 Etiope, G., Feyzullayev, A., and Baciu, C. L.: Terrestrial methane seeps and mud volcanoes: A global
344 perspective of gas origin, Mar. Pet. Geol., 26, 333–344, https://doi.org/10.1016/j.marpetgeo.2008.03.001,
345 2009.

346

347 Frankenberg, C., Platt, U., and Wagner, T.: Iterative maximum a posteriori (IMAP)-DOAS for retrieval
348 of strongly absorbing trace gases: Model studies for CH_4 and CO_2 retrieval from near infrared spectra of

https://doi.org/10.5194/amt-2020-51
Preprint. Discussion started: 12 May 2020

Atmospheric Measurement Techniques Discussions

SCIAMACHY onboard ENVISAT, Atmos. Chem. Phys., 5, 9–22, https://doi.org/10.5194/acp-5-9-2005, 2005.

Frankenberg, C., Thorpe, A. K., Thompson, D. R., Hulley, G., Kort, E. A., Vance, N., Borchardt, J., Krings, T., Gerilowski, K., Sweeney, C., Conley, S., Bue, B. D., Aubrey, A. D., Hook, S., and Green, R. O.: Airborne methane remote measurements reveal heavy-tail flux distribution in Four Corners region, Proc. Natl. Acad. Sci. U. S. A., 113, 9734–9739, https://doi.org/10.1073/pnas.1605617113, 2016.

Gao, B. C., Heidebrecht, K. B., and Goetz, A. F. H.: Derivation of scaled surface reflectances from AVIRIS data, Remote Sens. Environ., 44, 165–178, https://doi.org/10.1016/0034-4257(93)90014-O, 1993.

Gedney, N., Cox, P. M., and Huntingford, C.: Climate feedback from wetland methane emissions, Geophys. Res. Lett., 31, L20503. https://doi.org/10.1029/2004GL020919, 2004.

Green, R. O., Eastwood, M. L., Sarture, C. M., Chrien, T. G., Aronsson, M., Chippendale, B. J., Faust, J. A., Pavri, B. E., Chovit, C. J., Solis, M., Olah, M. R., and Williams, O.: Imaging spectroscopy and the Airborne Visible/Infrared Imaging Spectrometer (AVIRIS), Remote Sens. Environ., 65, 227–248, https://doi.org/10.1016/S0034-4257(98)00064-9, 1998.

He, L., Zeng, Z.-C., Pongetti, T. J., Wong, C., Liang, J., Gurney, K. R., Newman, S., Yadav, V., Verhulst, K., Miller, C. E., and Duren, R.: Atmospheric methane emissions correlate with natural gas consumption from residential and commercial sectors in Los Angeles, Geophys. Res. Lett., 46, 8563–8571, https://doi.org/10.1029/2019GL083400, 2019.

Henyey, L. G., and Greenstein, J. L.: Diffuse radiation in the galaxy, Astrophys. J., 93, 70–83, https://doi.org/10.1086/144246, 1941.

Herrero, M., Henderson, B., Havlík, P., Thornton, P. K., Conant, R. T., Smith, P., Wirsenius, S., Hristov, A. N., Gerber, P., Gill, M., Butterbach-Bahl, K., Valin, H., Garnett, T., and Shehfest, E.: Greenhouse gas mitigation potentials in the livestock sector, Nature Clim. Change, 6, 452–461, https://doi.org/10.1038/nclimate2925, 2016.

https://doi.org/10.5194/amt-2020-51
Preprint. Discussion started: 12 May 2020

Atmospheric Measurement Techniques Discussions

382 Holmes, C. D., Prather, M. J., Søvde, O. A., and Myhre, G.: Future methane, hydroxyl, and their
383 uncertainties: key climate and emission parameters for future predictions, Atmos. Chem. Phys., 13, 285–
384 302, https://doi.org/10.5194/acp-13-285-2013, 2013.
385
386 Howarth, R. W.: Methane emissions and climatic warming risk from hydraulic fracturing and shale gas
387 development: implications for policy, Energy and Emission Control Technologies, 3, 45–54,
388 https://doi.org/10.2147/EECT.S61539, 2015.
389
390 Howarth, R. W.: Ideas and perspectives: is shale gas a major driver of recent increase in global
391 atmospheric methane?, Biogeosciences, 16, 3033–3046, https://doi.org/10.5194/bg-16-3033-2019, 2019.
392
393 Howarth, R. W., Santoro, R., and Ingraffea, A.: Methane and the greenhouse gas footprint of natural gas
394 from shale formations, Clim. Change, 106, 679, https://doi.org/10.1007/s10584-011-0061-5, 2011.
395
396 Kalnay, E., Kanamitsu, M., Kistler, R., Collins, W., Deaven, D., Gandin, L., Iredell, M., Saha, S., White,
397 G., Woollen, J., Zhu, Y., Chelliah, M., Ebisuzaki, W., Higgins, W., Janowiak, J., Mo, K. C., Ropelewski,
398 C., Wang, J., Leetmaa, A., Reynolds, R., Jenne, R., and Joseph, D.: The NCEP/NCAR 40-year reanalysis
399 project, B. Am. Meteorol. Soc., 77, 437–471, https://doi.org/10.1175/1520-
400 0477(1996)077<0437:TNYRP>2.0.CO;2, 1996.
401
402 Kirschke, S., Bousquet, P., Ciais, P., Saunois, M., Canadell, Josep G., Dlugokencky. E. J., Bergamaschi,
403 P., Bergmann, D., Blake, D. R., Bruhwiler, L., Cameron-Smith, P., Castaldi, S., Chevallier, F., Feng, L.,
404 Fraser, A., Heimann, M, Hodson, E. L., Houweling, S., Josse, B., Fraser, P. J., Krummel, P. B., Lamarque,
405 J.-F., Langenfelds, R. L., Le Quere, C., Naik, V., O'Doherty, S., Palmer, P. I., Pison, I., Plummer, D.,
406 Poulter, B., Prinn, R. G., Rigby, M., Ringeval, B., Santini, M. Schmidt, M., Shindell, D. T., Simpson, I.
407 J., Spahni, R., Steele, L. P., Strode, S. A., Sudo, K., Szopa, S., van der Werf, G. R., Voulgarakis, A., van
408 Weele, M., Weiss, R. F., Williams, J. E., and Zeng, G.: Three decades of global methane sources and
409 sinks, Nature Geosci., 6, 813–823, https://doi.org/10.1038/ngeo1955, 2013.
410
411 Kort, E. A., Frankenberg, C., Costigan, K. R., Lindenmaier, R., Dubey, M. K., and Wunch, D.: Four
412 corners: the largest US methane anomaly viewed from space, Geophys. Res. Lett., 41, 6898–6903,
413 https://doi.org/10.1002/2014GL061503, 2014.
414

https://doi.org/10.5194/amt-2020-51
Preprint. Discussion started: 12 May 2020

Kruse, F.: Comparison of ATREM, ACORN, and FLAASH atmospheric corrections using low-altitude AVIRIS data of Boulder, CO, in: Summaries of 13th JPL Airborne Geoscience Workshop, Jet Propulsion Laboratory, Pasadena, CA, 2004.

Kvenvolden, K. A.: Methane hydrate – A major reservoir of carbon in the shallow geosphere, Chem. Geol., 71, 41–51, https://doi.org/10.1016/0009-2541(88)90104-0, 1998.

Kvenvolden, K. A., and Rogers, B. W.: Gaia's breath – global methane exhalations, Mar. Pet. Geol., 22, 579–590, https://doi.org/10.1016/j.marpetgeo.2004.08.004, 2005.

Macdonald, J. A., Fowler, D., Hargreaves, K. J., Skiba, U., Leith, I. D., and Murray, M. B.: Methane emission rates from a northern wetland; response to temperature, water table and transport, Atmos. Environ., 32, 3219–3227, https://doi.org/10.1016/S1352-2310(97)00464-0, 1998.

Manolakis, D., Truslow, E., Pieper, M., Cooley, T., and Brueggeman, M.: Detection algorithms in hyperspectral imaging systems: An overview of practical algorithms, IEEE Signal Proc. Mag., 31, 24–33, https://doi.org/10.1109/MSP.2013.2278915, 2014.

Merchant, C. J., Le Borgne, P., Roquet, H., and Legendre, G.: Extended optimal estimation techniques for sea surface temperature from the Spinning Enhanced Visible and Infra-Red Imager (SEVIRI), Remote Sens. Environ., 131, 287–297, https://doi.org/10.1016/j.rse.2012.12.019, 2013.

Myhre, G., Shindell, D., Bréon, F.-M., Collins, W., Fuglestvedt, J., Huang, J., Koch, D., Lamarque, J.-F., Lee, D., Mendoza, B., Nakajima, T., Robock, A., Stephens, G., Takemura, T., and Zhang, H.: Anthropogenic and Natural Radiative Forcing, Climate Change 2013: The Physical Science Basis. Contribution of Working Group I to the Fifth Assessment Report of the Intergovernmental Panel on Climate Change – IPCC, 2013.

Nisbet, E. G., Dlugokencky, E, J., and Bousquet, P.: Methane on the rise-again, Science, 343, 493–495, https//doi.org/10.1126/science.1247828, 2014.

Nisbet, E. G., Dlugokencky, E. J., Manning, M. R., Lowry, D., Fisher, R. E., France, J. L., Michel, S. E., Miller, J. B., White, J. W. C., Vaughn, B., Bousquet, P., Pyle, J. A., Warwick, N. J., Cain, M., Brownlow,

https://doi.org/10.5194/amt-2020-51
Preprint. Discussion started: 12 May 2020

448 R., Zazzeri, G., Lanoisellé, M., Manning, A. C., Gloor, E., Worthy, D. E. J., Brunke, E.-G., Labuschagne,
449 C., Wolff, E. W., and Ganesan, A. L.: Rising atmospheric methane: 2007–2014 growth and isotopic shift,
450 Glob. Biogeochem. Cycles, 30, 1356–1370, https://doi.org/10.1002/2016GB005406, 2016.
451
452 O'Dell, C. W., Eldering, A., Wennberg, P. O., Crisp, D., Gunson, M. R., Fisher, B., Frankenberg, C.,
453 Kiel, M., Lindqvist, H., Mandrake, L., Merrelli, A., Natraj, V., Nelson, R. R., Osterman, G. B., Payne,
454 V. H., Taylor, T. E., Wunch, D., Drouin, B. J., Oyafuso, F., Chang, A., McDuffie, J., Smyth, M., Baker,
455 D. F., Basu, S., Chevallier, F., Crowell, S. M. R., Feng, L., Palmer, P. I., Dubey, M., García, O. E.,
456 Griffith, D. W. T., Hase, F., Iraci, L. T., Kivi, R., Morino, I., Notholt, J., Ohyama, H., Petri, C., Roehl,
457 C. M., Sha, M. K., Strong, K., Sussmann, R., Te, Y., Uchino, O. and Velazco, V. A.: Improved retrievals
458 of carbon dioxide from Orbiting Carbon Observatory-2 with the version 8 ACOS algorithm, Atmos.
459 Meas. Tech., 11(12), 6539–6576, https://doi.org/10.5194/amt-11-6539-2018, 2018
460
461 Perkins, T., Adler-Golden, S. M., Matthew, M. W., Berk, A., Bernstein, L. S., Lee, J., Fox M.: Speed
462 and accuracy improvements in FLAASH atmospheric correction of hyperspectral imagery, Opt. Eng.,
463 51, 111707, https://doi.org/10.1117/1.OE.51.11.111707, 2012.
464
465 Qu, Z., Kindel, B. C., and Goetz, A. F. H.: The high accuracy atmospheric correction for hyperspectral
466 data (HATCH) model, IEEE Trans. Geosci. Remote Sens., 41, 1223–1231,
467 https://doi.org/10.1109/TGRS.2003.813125, 2003.
468
469 Richter, R.: Atmospheric correction of DAIS hyperspectral image data, Comput. Geosci., 22, 785–793,
470 https://doi.org/10.1016/0098-3004(96)00016-7, 1996.
471
472 Richter, R.: Correction of satellite imagery over mountainous terrain, Appl. Opt., 37, 4004–4015,
473 https://doi.org/10.1364/AO.37.004004, 1998.
474
475 Richter, R., and Schläpfer, D.: Geo-atmospheric processing of airborne imaging spectrometry data. Part
476 2: Atmospheric/topographic correction, Int. J. Remote Sens., 23, 2631–2649,
477 https://doi.org/10.1080/01431160110115834, 2002.
478

https://doi.org/10.5194/amt-2020-51
Preprint. Discussion started: 12 May 2020

Atmospheric Measurement Techniques Discussions

479 Roberts, D. A., Bradley, E. S., Cheung, R., Leifer, I., Dennison, P. E., and Margolis, J. S.: Mapping
480 methane emissions from a marine geological seep source using imaging spectrometry, Remote Sens.
481 Environ., 114, 592–606, https://doi.org/10.1016/j.rse.2009.10.015, 2010.
482
483 Rodgers, C. D.: Inverse Methods for Atmospheric Sounding: Theory and Practice, World Scientific,
484 Singapore, 2000.
485
486 Rothman, L. S., Gordon, I. E., Barbe, A., Benner, D. C., Bernath, P. E., Birk, M., Boudon, V., Brown,
487 L. R., Campargue, A., Champion, J. P., Chance, K., Coudert, L. H., Dana, V., Devi, V. M., Fally, S.,
488 Flaud, J. M., Gamache, R. R., Goldman, A., Jacquemart, D., Kleiner, I., Lacome, N., Lafferty, W. J.,
489 Mandin, J. Y., Massie, S. T., Mikhailenko, S. N., Miller, C. E., Moazzen-Ahmadi, N., Naumenko, O. V.,
490 Nikitin, A. V., Orphal, J., Perevalov, V. I., Perrin, A., Predoi-Cross, A., Rinsland, C. P., Rotger, M.,
491 Šimečková, M., Smith, M. A. H., Sung, K., Tashkun, S. A., Tennyson, J., Toth, R. A., Vandaele, A. C.,
492 and Vander Auwera, J.: The HITRAN 2008 molecular spectroscopic database, J. Quant. Spectrosc.
493 Radiat. Transfer, 110, 533–572, https://doi.org/10.1016/j.jqsrt.2009.02.013, 2009.
494
495 Schaefer, H., Fletcher, S. E. M., Veidt, C., Lassey, K. R., Brailsford, G. W., Bromley, T. M.,
496 Dlugokencky, E. J., Michel, S. E., Miller, J. M., Levin, I., Lowe, D. C., Martin, R. J., Vaughn, B. H., and
497 White, J. W. C.: A 21st-century shift from fossil-fuel to biogenic methane emissions indicated by $^{13}CH_4$,
498 Science, 352, 80-84, https://doi.org/10.1126/science.aad2705, 2016.
499
500 Schaefer, K., Lantuit, H., Romanovsky, V. E., Schuur, E. A. G., and Witt, R.: The impact of the
501 permafrost carbon feedback on global climate, Environ. Res. Lett., 9, 085003,
502 https://doi.org/10.1088/1748-9326/9/8/085003, 2014.
503
504 Schaepman, M. E., Ustin, S. L., Plaza, A. J., Painter, T. H., Verrelst, J., and Liang, S.: Earth system
505 science related imaging spectroscopy—An assessment, Remote Sens. Environ., 113, S123–S137,
506 https://doi.org/10.1016/j.rse.2009.03.001, 2009.
507
508 Schuur, E. A. G., McGuire, A. D., Schädel, C., Grosse, G., Harden, J. W., Hayes, D. J., Hugelius, G.,
509 Koven, C. D., Kuhry, P., Lawrence, D. M., Natali, S. M., Olefeldt, D., Romanovsky, V. E., Schaefer, K.,
510 Turetsky, M. R., Treat, C. C., and Vonk, J. E.: Climate change and the permafrost carbon feedback,
511 Nature, 520, 171–179, https://doi.org/10.1038/nature14338, 2015.

https://doi.org/10.5194/amt-2020-51
Preprint. Discussion started: 12 May 2020

512 Seinfeld, J. H., and Pandis, S. N.: Atmospheric Chemistry and Physics: From Air Pollution to Climate
513 Change, Wiley, New Jersey, USA, 2006.
514
515 Spurr, R., and Natraj, V.: A linearized two-stream radiative transfer code for fast approximation of
516 multiple-scatter fields, J. Quant. Spectrosc. Radiat. Transfer, 112, 2630–2637,
517 https://doi.org/10.1016/j.jqsrt.2011.06.014, 2011.
518
519 Staenz, K., Szeredi, T., and Schwarz, J.: ISDAS — A system for processing/analyzing hyperspectral data,
520 Can. J. Remote Sens., 24, 99–113, https://doi.org/10.1080/07038992.1998.10855230, 1998.
521
522 Themelis, N. J., and Ulloa, P. A.: Methane generation in landfills, Renewable Energy, 32, 1243–1257,
523 https://doi.org/10.1016/j.renene.2006.04.020, 2007.
524
525 Thompson, D. R., Leifer, I., Bovensmann, H., Eastwood, M., Fladeland, M., Frankenberg, C.,
526 Gerilowski, K., Green, R. O., Kratwurst, S., Krings, T., Luna, B., and Thorpe, A. K.: Real-time remote
527 detection and measurement for airborne imaging spectroscopy: a case study with methane, Atmos. Meas.
528 Tech., 8, 4383–4397, https://doi.org/10.5194/amt-8-4383-2015, 2015.
529
530 Thorpe, A. K., Frankenberg, C., and Roberts, D. A.: Retrieval techniques for airborne imaging of
531 methane concentrations using high spatial and moderate spectral resolution: Application to AVIRIS,
532 Atmos. Meas. Tech., 7, 491–506, https://doi.org/10.5194/amt-7-491-2014, 2014.
533
534 Thorpe, A. K., Roberts, D. A., Bradley, E. S., Funk, C. C., Dennison, P. E., and Leifer, I.: High resolution
535 mapping of methane emissions from marine and terrestrial sources using a Cluster-Tuned Matched Filter
536 technique and imaging spectrometry, Remote Sens. Environ., 134, 305–318,
537 https://doi.org/10.1016/j.rse.2013.03.018, 2013.
538
539 Walter, K. M., Zimov, S. A., Chanton, J. P., Verbyla, D., and Chapin III, F. S.: Methane bubbling from
540 Siberian thaw lakes as a positive feedback to climate warming, Nature, 443, 71–75,
541 https://doi.org/10.1038/nature05040, 2006.
542

https://doi.org/10.5194/amt-2020-51
Preprint. Discussion started: 12 May 2020

543 Woodwell, G. M., Mackenzie, F. T., Houghton, R. A., Apps, M., Gorham, E., and Davidson, E.: Biotic
544 feedbacks in the warming of the earth, Climatic Change, 40, 495–518,
545 https://doi.org/10.1023/A:1005345429236, 1998.
546
547 Xi, X., Natraj, V., Shia, R. L., Luo, M., Zhang, Q., Newman, S., Sander, S. P., and Yung, Y. L.: Simulated
548 retrievals for the remote sensing of CO_2, CH_4, CO, and H_2O from geostationary orbit, Atmos. Meas. Tech.,
549 8, 4817–4830, https://doi.org/10.5194/amtd-8-5809-2015, 2015.
550
551 Yoshida, Y., Kikuchi, N., Morino, I., Uchino, O., Oshchepkov, S., Bril, A., Saeki, T., Schutgens, N.,
552 Toon, G. C., Wunch, D., Roehl, C. M., Wennberg, P. O., Griffith, D. W. T., Deutscher, N. M., Warneke,
553 T., Notholt, J., Robinson, J., Sherlock, V., Connor, B., Rettinger, M., Sussmann, R., Ahonen, P.,
554 Heikkinen, P., Kyrö, E., Mendonca, J., Strong, K., Hase, F., Dohe, S., and Yokota, T.: Improvement of
555 the retrieval algorithm for GOSAT SWIR XCO_2 and XCH_4 and their validation using TCCON data,
556 Atmos. Meas. Tech., 6, 1533–1547, https://doi.org/10.5194/amt-6-1533-2013, 2013.
557
558 Zeng, Z.-C., Zhang, Q., Natraj, V., Margolis, J. S., Shia, R. -L., Newman, S., Fu, D., Pongetti, T. J.,
559 Wong, K. W., Sander, S. P., Wennberg, P. O., and Yung, Y. L.: Aerosol scattering effects on water vapor
560 retrievals over the Los Angeles Basin, Atmos. Chem. Phys., 17, 2495–2508, https://doi.org/10.5194/acp-
561 17-2495-2017, 2017.
562
563 Zeng, Z.-C., Natraj, V., Xu, F., Pongetti, T. J., Shia, R.-L., Kort, E. A., Toon, G. C., Sander, S. P., and
564 Yung, Y. L.: Constraining aerosol vertical profile in the boundary layer using hyperspectral
565 measurements of oxygen absorption, Geophys. Res. Lett., 45, 10772–10780,
566 https://doi.org/10.1029/2018GL079286, 2018.
567
568 Zhang, Q., Natraj, V., Li, K. -F., Shia, R. -L., Fu, D., Pongetti, T. J., Sander S. P., Roehl, C. M., and
569 Yung, Y. L.: Accounting for aerosol scattering in the CLARS retrieval of column averaged CO_2 mixing
570 ratios, J. Geophys. Res., 120, 7205–7218, https://doi.org/10.1002/2015JD023499, 2015.
571
572 Zhang, Q., Shia, R. -L., Sander, S. P., and Yung, Y. L.: X_{CO_2} retrieval error over deserts near critical surface
573 albedo, Earth Space Sci., 2, 1–10, https://doi.org/10.1002/2015EA000143, 2016.
574

https://doi.org/10.5194/amt-2020-51
Preprint. Discussion started: 12 May 2020

Atmospheric Measurement Techniques Discussions

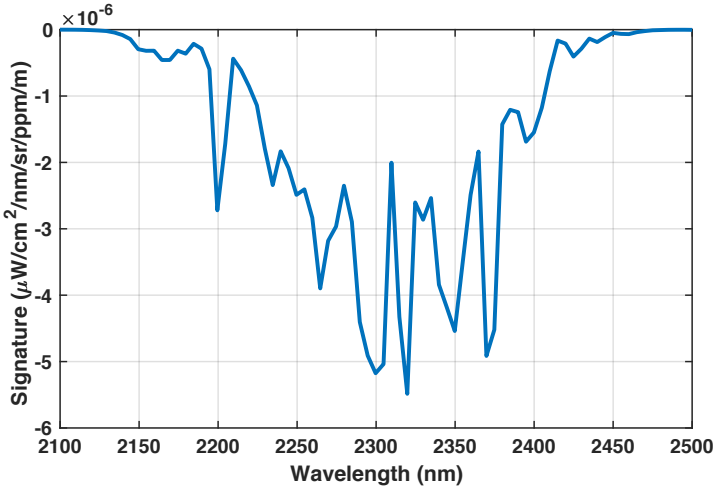

Figure 1: The target signature used for the Matched Filter method.

https://doi.org/10.5194/amt-2020-51
Preprint. Discussion started: 12 May 2020

Atmospheric Measurement Techniques Discussions

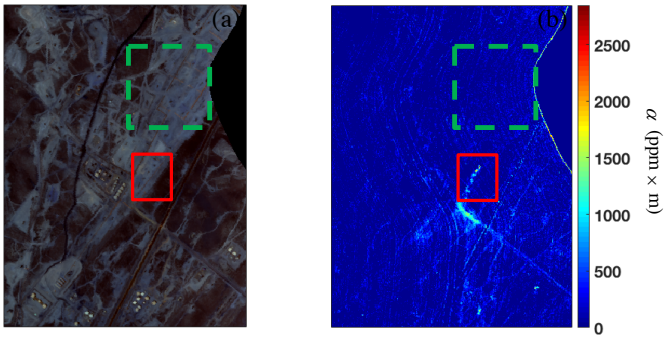

Figure 2: (a) RGB image of flight data from 4 September 2014 (ang20140904t204546). Adapted from Thompson et al. (2015). (b) CH_4 enhancement value α (ppm × m) obtained by the MF method. An emission source is shown in the solid red box and the background region near the target for the MF calculation is indicated by the dashed green box.

https://doi.org/10.5194/amt-2020-51
Preprint. Discussion started: 12 May 2020

Atmospheric Measurement Techniques Discussions

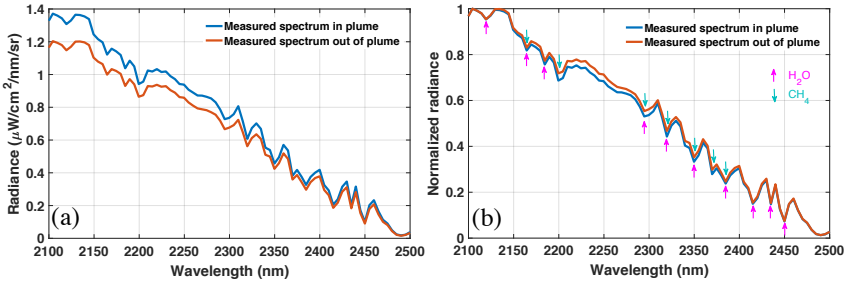

Figure 3: (a) Real radiance and (b) normalized radiance at cross-track detector elements (in and out of plume) from the sample AVIRIS-NG measurement. The colored arrows in (b) show the main absorption features due to H_2O (purple) and CH_4 (green).

https://doi.org/10.5194/amt-2020-51
Preprint. Discussion started: 12 May 2020

Atmospheric Measurement Techniques Discussions

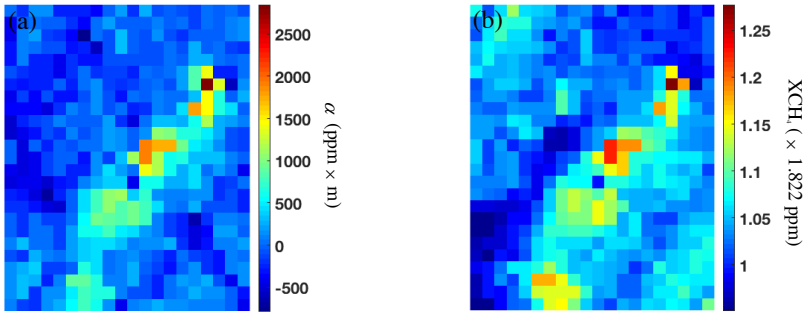

Figure 4: Retrieval image for the plume center (500 elements) based on the (a) MF method and (b) OE method.

https://doi.org/10.5194/amt-2020-51
Preprint. Discussion started: 12 May 2020

Atmospheric Measurement Techniques Discussions

597

598

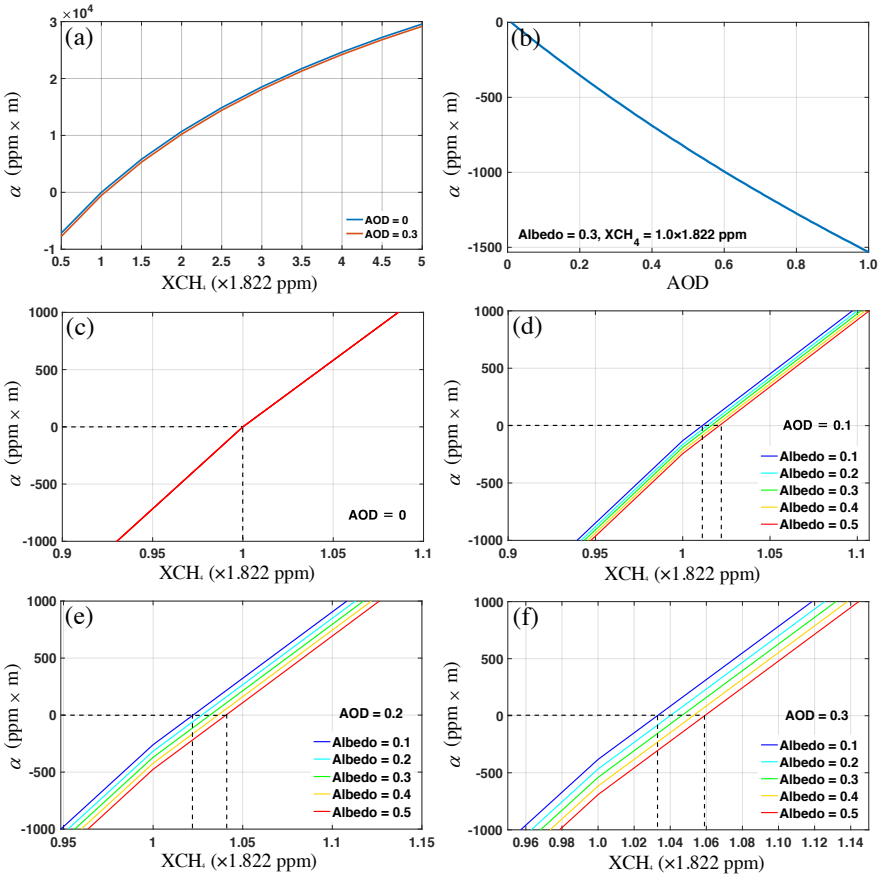

599 **Figure 5: (a) α as a function of XCH_4 for AOD = 0 and AOD = 0.3 (surface albedo = 0.3). (b) α as a function**

600 **of AOD (XCH_4 = 1.0 × 1.822 ppm, surface albedo = 0.3). Zoomed in versions of α as a function of XCH_4 for**

601 **different albedos (0.1-0.5), where (c) AOD = 0, (d) AOD = 0.1, (e) AOD = 0.2, and (f) AOD = 0.3.**

602

https://doi.org/10.5194/amt-2020-51
Preprint. Discussion started: 12 May 2020

Atmospheric Measurement Techniques Discussions

603

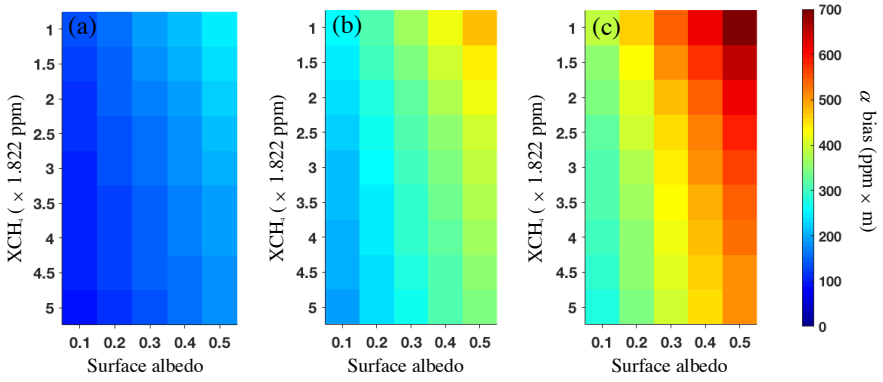

604

605 **Figure 6: Bias in α as a function of XCH_4 and surface albedo for (a) AOD = 0.1, (b) AOD = 0.2, and (c) AOD**

606 **= 0.3.**

607

https://doi.org/10.5194/amt-2020-51
Preprint. Discussion started: 12 May 2020

Atmospheric Measurement Techniques Discussions

608

609

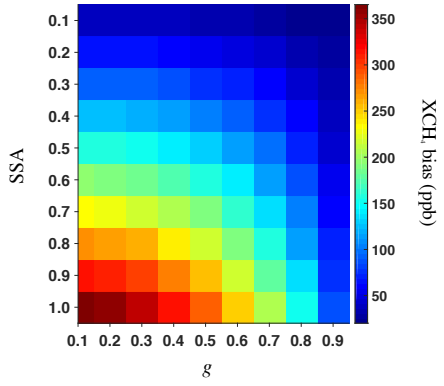

610 **Figure 7: CH_4 retrieval biases for different values of *g* and SSA. Albedo, AOD = 0.3, XCH_4 = 1.0 × 1.822 ppm.**

https://doi.org/10.5194/amt-2020-51
Preprint. Discussion started: 12 May 2020

Atmospheric Measurement Techniques Discussions

611

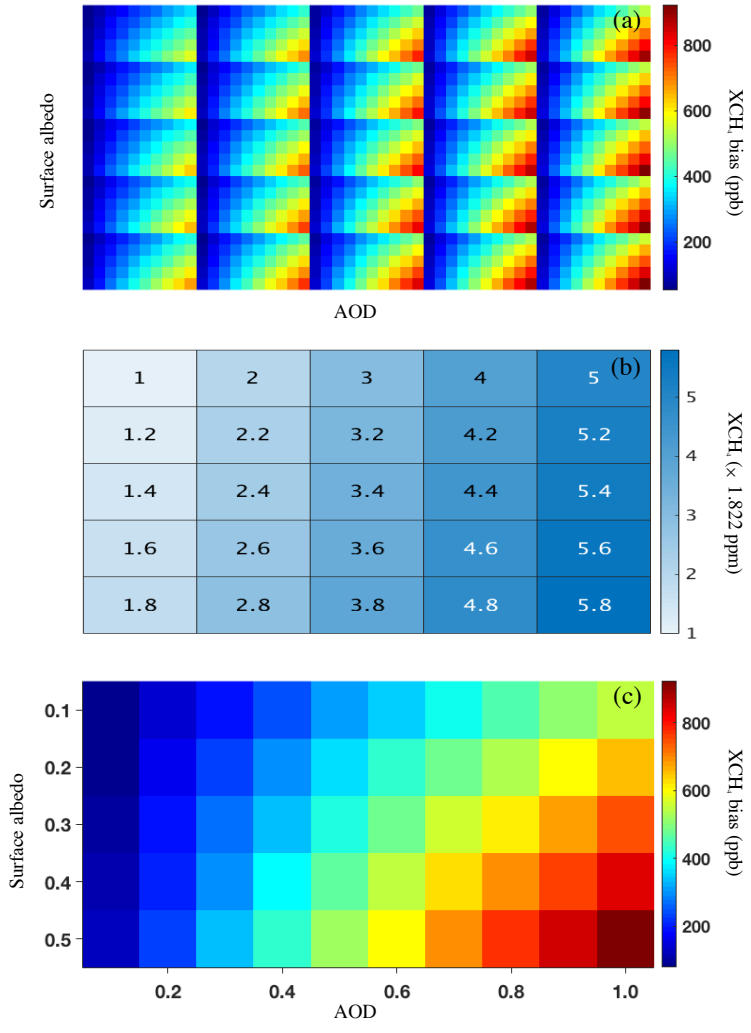

612

613 **Figure 8: (a) Bias in retrieved XCH$_4$ for different values of XCH$_4$, AOD and surface albedo. g = 0.75, SSA =**
614 **0.95. (b) XCH$_4$ for each box in (a). (c) Zoomed in plot of bottom right box (XCH$_4$ = 5.8 × 1.822 ppm). The x**
615 **and y axes show the variation of AOD and surface albedo, respectively. These changes are identical for every**
616 **box in (a).**

617

https://doi.org/10.5194/amt-2020-51
Preprint. Discussion started: 12 May 2020

Atmospheric Measurement Techniques Discussions

618

619

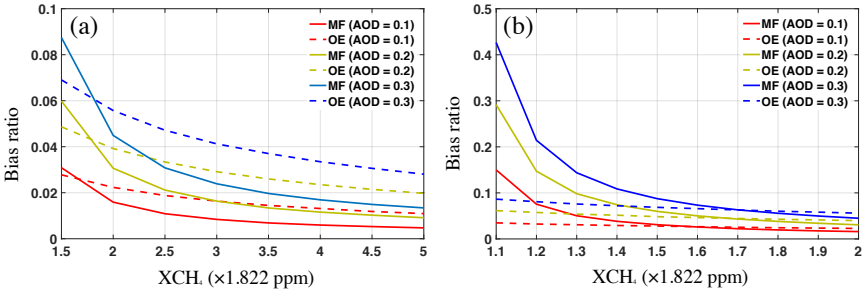

620 **Figure 9: (a) Bias ratio as a function of CH_4 concentration for the two retrieval techniques, where the XCH_4**
621 **ranges from 1.5 to 5 (× 1.822 ppm). (b) Same as (a), but for XCH_4 ranging from 1.1 to 2 (× 1.822 ppm). Surface**
622 **albedo is set to 0.3 for all cases; results for the MF and OE methods are shown by solid and dashed lines,**
623 **respectively.**

624

https://doi.org/10.5194/amt-2020-51
Preprint. Discussion started: 12 May 2020

Atmospheric Measurement Techniques Discussions

625

Attribute	Values
Sensor height	1 km
View zenith angle	11.91°
Solar zenith angle	30.75°
Relative azimuth angle	22.87°
Aerosol loading region	from surface to 1 km
SSA	0.95
g	0.75

626 **Table 1: Inputs for the 2S-ESS model simulation.**